# Ultrafast high-resolution multi-parametric brain MRI using 3D Echo Planar Time-resolved Imaging

Fuyixue Wang[1,2†*], Zijing Dong[1,3†], Timothy G. Reese[1,4], Bruce Rosen[1,2,4], Lawrence L. Wald[1,2,4], Kawin Setsompop[1,2,4]

[1]*Athinoula A. Martinos Center for Biomedical Imaging, Massachusetts General Hospital, Charlestown, Massachusetts, USA*

[2]*Harvard-MIT Health Sciences and Technology, MIT, Cambridge, Massachusetts, USA*

[3]*Department of Electrical Engineering and Computer Science, MIT, Cambridge, Massachusetts, USA*

[4]*Department of Radiology, Harvard Medical School, USA*

---

***Correspondence to:**

Fuyixue Wang,
Athinoula A. Martinos Center for Biomedical Imaging
Charlestown, MA, 02129
United States
Email: fwang18@mgh.harvard.edu

[†]These authors contribute equally to the manuscript.

## Abstract

Multi-parametric quantitative MRI has shown great potential to improve the sensitivity and specificity of clinical diagnosis, but suffers from impractical scan time especially at high spatial resolution, a major limiting factor that prevents it from common use. To address this long-standing challenge, we introduce a novel approach, termed 3D Echo Planar Time-resolved Imaging (3D-EPTI), which significantly increases the acceleration capacity of MRI sampling, and provides unprecedented acquisition efficiency for multi-parametric MRI. The high acceleration capability in 3D-EPTI is achieved by exploiting the spatiotemporal correlation of MRI data at multiple timescales through new encoding strategies within and between its efficient continuous data readouts. This has enabled robust and repeatable whole-brain multi-parametric mapping at high isotropic resolution within minutes. 3D-EPTI may greatly facilitate the clinical adoption of quantitative MRI and push towards the next-generation of brain examination with high efficacy and accuracy for improved diagnosis and longitudinal monitoring. Moreover, 3D-EPTI also offers a powerful tool for fast and repeatable submillimeter multi-parametric imaging that can be used to study detailed brain intra-cortical architectures for neuroscientific research.

## 1. Introduction

Multiparametric MRI provides quantitative measurements that are sensitive to a variety of tissue properties of the human brain. Its quantitative nature leads to less reliance on system conditions and human interpretation compared to standard qualitative images, and therefore has a great potential to improve the accuracy and efficacy of clinical diagnosis[1]. This improvement has been demonstrated in a wide range of diseases, such as epilepsy[2,3], brain tumor[4,5], multiple-sclerosis[6-8] and Alzheimer[9,10]. In addition, the quantitative measurements make it possible to measure the difference of tissue properties among different populations and along time, which is critical for understanding neurological diseases, brain development, and aging[11-13].

A major limitation of quantitative MRI is its long acquisition time. The common approach to measure quantitative parameters is to perform a model fitting using a series of qualitative images with different contrast weightings. Traditionally, long imaging time is needed for the acquisition of a single weighted image to fulfill the Shannon-Nyquist sampling theorem in the frequency (*k*-space) domain. This is dramatically exacerbated in quantitative MRI due to the need to acquire multiple contrast weightings, and even further in multi-parametric imaging due to the need to repeat such process for each parameter, leading to extremely long scan times. To accelerate the acquisition, undersampling in the frequency domain has been made possible by taking advantage of the spatial information provided by multi-channel coil arrays[14-16] or by enforcing prior knowledge of image properties, such as through compressed-sensing theory[17]. However, despite continuous efforts, the ability to accelerate sampling without compromising the image quality is still limited and obtaining multi-parametric MRI in clinical acceptable time remains a major challenge.

In this work, we introduce a novel method, termed 3D-Echo Planar Time-Resolved Imaging (3D-EPTI), that solves this long-lasting problem by enabling unprecedented acceleration and significantly improved imaging efficiency for multi-parametric imaging. By pushing multi-parametric MRI into an unprecedented fast regime (as short as 1 minute), 3D-EPTI should help facilitate a paradigm shift from qualitative to quantitative imaging in clinical practice, and also open up the possibility of acquiring multi-parametric maps at submillimeter isotropic resolution within a few minutes to reveal exquisite brain structures for neuroscientific research. With richer and more reproducible information obtained within a single scan, 3D-EPTI has the potential to increase patient throughput, patient compliance and cost effectiveness, paving the way for large-scale studies to establish new quantitative biomarkers for neurological diseases.

3D-EPTI pushes the limit of acceleration by exploiting the signal correlation in the spatiotemporal domain. The use of spatiotemporal correlation to achieve high acceleration for quantitative MRI has been an emerging area of research. Recent studies, such as MR fingerprinting[18-20] and MR multitasking[21], have utilized spatiotemporal correlation between readouts after different contrast-modulated excitations to accelerate multi-parametric imaging, which have shown promising results especially when used in conjunction with the low-rank subspace model[21-23]. In pursuit of a significant further increase in acceleration capability over state-of-the-art approaches, 3D-EPTI has been designed from the ground up to exploit stronger spatiotemporal correlations by developing: i) a new efficient continuous readout scheme, and ii) a data sampling strategy that takes

advantage of the correlation at multiple timescales, both within and between its continuous readouts.

The continuous readout scheme distinguishes 3D-EPTI from other quantitative MRI methods not only by its higher readout efficiency with minimal dead time, but also through exploiting the correlation between data sampled at a much shorter timescale (submillisecond) within the readout, to help with data reconstruction. At this timescale, only minimal phase accumulation and signal decay will occur, which lead to stronger temporal correlation. This stronger correlation can significantly increase the ability to recover highly undersampled data, and therefore pushes the boundaries of the acceleration to an unprecedented level. Previously, despite the exceptional efficiency, the continuous readout has mainly been used in the echo planar imaging (EPI) acquisition[24], where all signals across the readout are combined to form a single image without exploiting the spatiotemporal correlation within it. This limits its acceleration capacity, makes it difficult to acquire multiple images at a short time interval to track signal evolution for quantitative MRI, and also leads to severe image distortion and blurring by combining signals with different phase and magnitude. By exploiting the spatiotemporal correlation within the readout, 3D-EPTI is able to resolve a series of multi-contrast 3D images across the readout instead of just one single image at a high acceleration rate, providing continuous tracking of the signal evolution to fit the quantitative parameters. On the other hand, it ensures that each resolved image is formed by signals with the same phase and magnitude, eliminating the undesirable image distortion and blurring.

The second unique feature of 3D-EPTI is its new controlled- and incoherent-aliasing encoding schemes in the 4D spatiotemporal domain, which seamlessly integrates the use of the temporal correlation and the use of spatial information provided by multi-channel coil arrays. Here, data correlations at multiple timescales are exploited. Within readouts, a spatiotemporal encoding is designed by extending the controlled-aliasing approach[25,26] into the spatiotemporal domain. Conventionally, controlled-aliasing theory improves the ability to recover undersampled data by using a complementary spatial encoding strategy that better exploits the coil sensitivity. In 3D-EPTI, the complementary sampling is employed in the time dimension in addition to the spatial dimensions, increasing the ability to take advantage of both the spatial information provided by multi-channel coil arrays and the temporal correlation across adjacent signals, offering remarkably higher acceleration capacity (e.g., 80×) in the spatiotemporal space. Between readouts, a novel radial-block encoding is developed to exploit their correlation in a long timescale based on the compressed sensing theory[17]. The radial-block sampling creates incoherent aliasing along time that can be well excluded from the coherent signal evolutions, therefore provides another 10× acceleration. The combination of spatiotemporal CAIPI and radial-block undersampling offers a remarkable ~800× acceleration in the spatiotemporal domain.

The harmonious integration of the continuous readout and the novel intra- and inter-readout spatiotemporal encoding in 3D-EPTI provides unique datasets that allow us to time-resolve thousands of multi-contrast 3D images by enforcing the spatiotemporal correlation in the reconstruction process. This acquisition scheme can be applied to any sequence with different contrast-modulated radiofrequency (RF) pulses, or be adapted to other types of readouts to accurately track the signal evolution, and therefore is suitable for measuring a variety of quantitative parameters. This proof-of-concept work employs specific sequences to simultaneously obtain MR relaxation time constants $T_1$, $T_2$, $T_2^*$ as well as RF field ($B_1^+$) and proton density (PD). We demonstrated the

ability of 3D-EPTI to acquire high-quality whole-brain multi-parametric maps at isotropic 1.5-mm in 1 minute or at isotropic 1-mm in 3 minutes, which could take hours to acquire using standard acquisitions or tens of minutes using the state-of-the-art methods. This illustrates the potential of 3D-EPTI to enable the next-generation of clinical brain exams with ultra-fast speed and high repeatability. An isotropic 0.7-mm 3D-EPTI protocol was also developed to allow, for the first time, the examination of simultaneously acquired $T_1$, $T_2$, and $T_2^*$ in less than 10 minutes to investigate the intra-cortical architecture. Finally, we also present multiple contrast-weighted images synthesized from the high-quality 3D-EPTI quantitative maps, offering optimal visualization with arbitrary views and adjustable contrast weightings.

## 2. Results

**Efficient 3D-EPTI imaging framework.**

Figure 1 shows a detailed framework of the 3D-EPTI acquisition. An inversion-recovery gradient echo (IR-GE) and a variable-flip-angle gradient-and-spin-echo[27] (VFA-GRASE) sequence (Fig. 1a) were chosen and carefully optimized to provide signal evolutions that are sensitive to $T_1$, $T_2$, and $T_2^*$ relaxations (Fig. 1b). After each RF excitation, a 3D-EPTI readout is acquired, which continuously captures the temporal signal evolution with efficient bipolar gradient. To resolve images within the readout with high acceleration, a spatiotemporal CAIPI encoding is employed in a 4D spatiotemporal (*k*-*t*) domain (Fig. 1d, the readout dimension $k_x$ is fully-sampled and therefore omitted in the illustration). At each time point within the readout, a particular phase and partition position ($k_y$-$k_z$) is acquired in the frequency domain that is interleaved to its neighboring time points in a 'controlled-aliasing' pattern. Across a slightly longer timescale, two complementary CAIPI patterns are interleaved across echoes (orange and green points in Fig. 1d) to provide more independent *k*-space sampling locations. Each 3D-EPTI readout covers a relatively small block in $k_y$-$k_z$-$t$ space to ensure that the neighboring $k_y$-$k_z$ samplings are close in time. The 'controlled aliasing' pattern, the complementary sampling across echoes, and the proximity in time together result in high spatiotemporal correlation and allow effective use of the available coil sensitivity information. Therefore, the highly-undersampled data (e.g., undersampling rate = 80×) at each time point can be easily reconstructed, resolving a series images across the readout at a submillisecond time interval (Fig. 1d, left).

In each repetition time (TR), multiple *k*-*t* blocks can be acquired across multiple readouts after different excitations (Fig. 1c, blocks in the same color are acquired in the same TR). To quickly encode the 4D *k*-*t* space using a small number of TRs, a golden-angle radial-block Cartesian sampling is employed across the readouts. Specifically, the blocks acquired after the same excitation form a diagonal radial blade in the phase-partition encoding ($k_y$-$k_z$) space, with different blade angulations across different readouts. This is developed to create a favorable spatiotemporal incoherent aliasing across the readouts for constrained reconstruction, that permits a further ~10× acceleration through acquiring only a few blades for each readout instead of the full $k_y$-$k_z$ sampling.

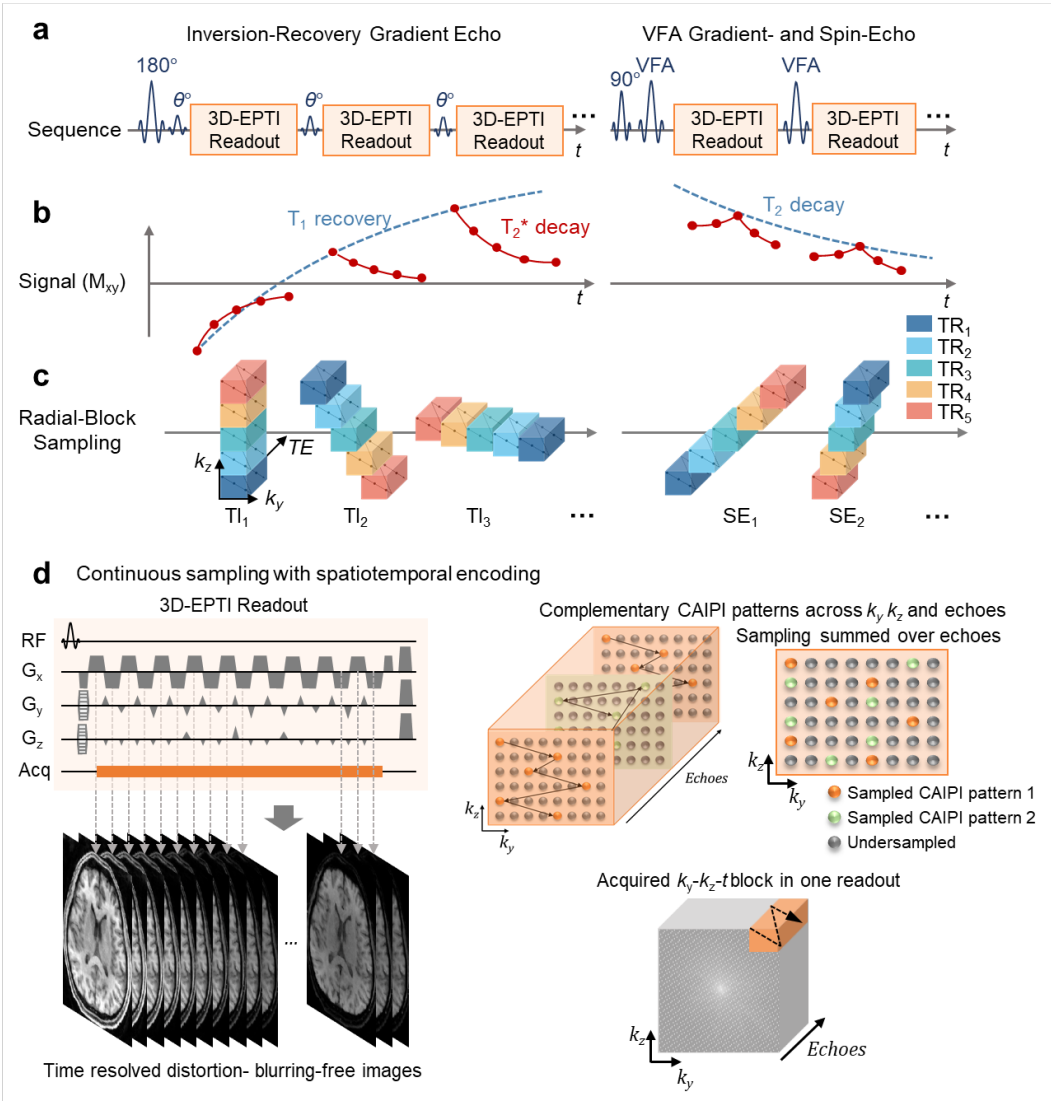


Figure 1. Illustration of the 3D-EPTI acquisition. **a**, The sequence diagrams of the inversion-recovery gradient-echo (IR-GE) and the variable-flip-angle gradient and spin-echo (VFA-GRASE) sequences with 3D-EPTI readouts at each inversion time (TI) and spin-echo (SE). **b**, The designed sequence provides signal evolutions with high sensitivity to $T_1$, $T_2$ and $T_2^*$ relaxation, which can be continuously tracked by the 3D-EPTI sampling. **c**, Instead of acquiring data across the full frequency space ($k_y$-$k_z$) at every TI or SE, a radial-block sampling pattern is utilized, which creates spatiotemporal incoherent aliasing across the readouts for constrained reconstruction and permits ~10× acceleration. The blocks acquired in different TRs are color-coded. **d**, Details of the continuous bipolar readout with an optimized spatiotemporal CAIPI encoding used to efficiently covers a $k_y$-$k_z$-$t$ block per 3D-EPTI readout. The neighboring data points are acquired close in time to create strong temporal correlation. Two CAIPI patterns (orange and green points) are utilized in a complementary fashion across the echoes to provide additional complementary sampling. The combination of spatiotemporal CAIPI and radial-block undersampling offers a remarkable ~800× acceleration in the spatiotemporal domain, that enables fast acquisition of more than a thousand multi-contrast images within a few TRs. Note that the readout ($k_x$) dimension is fully-sampled and therefore omitted in the illustration.

The acquired highly undersampled data, with carefully designed spatiotemporal encoding patterns that fully exploit the spatiotemporal correlation, were then reconstructed by a low-rank subspace reconstruction, tailored specifically to 3D-EPTI to time-resolve thousands of multi-contrast images (Supplementary Fig. 1). The low-rank subspace method[22] was chosen for use based on its superior ability to improve the conditioning

in the reconstruction by utilizing the low-rank prior information of the signal evolution, therefore achieving high image SNR[22,28-33]. Finally, the quantitative values were obtained by matching the signal evolution with a pre-calculated dictionary.

**Simultaneous $T_1$, $T_2$, and $T_2^*$ mapping in 3-minutes at 1-mm isotropic resolution.**

$T_1$, $T_2$ and $T_2^*$ are different MR relaxation time constants that provide characteristic information of the underlying tissue properties. $T_1$ has been demonstrated to be sensitive to myelin concentration[34] and axon diameter[35], providing excellent white-gray matter contrast[36] and high sensitivity for evaluating pathologies such as demyelination[37]. $T_2^*$ can detect changes in iron concentrations that have been observed in many neurological disorders[38-40]. $T_2$ is affected by myelin[41] and iron concentrations as well, and is also sensitive to abnormal fluids in the tissue which can be used to characterize inflammation and edema[42]. Therefore, the simultaneous acquisition of these three parameters will provide complementary information to improve the sensitivity and specificity in evaluating the heterogeneous properties of human brain. Further, recent studies have shown that analysis performed using a combination of quantitative parameters could help disentangle contributing signals from molecular and water compositions in the brain[13].

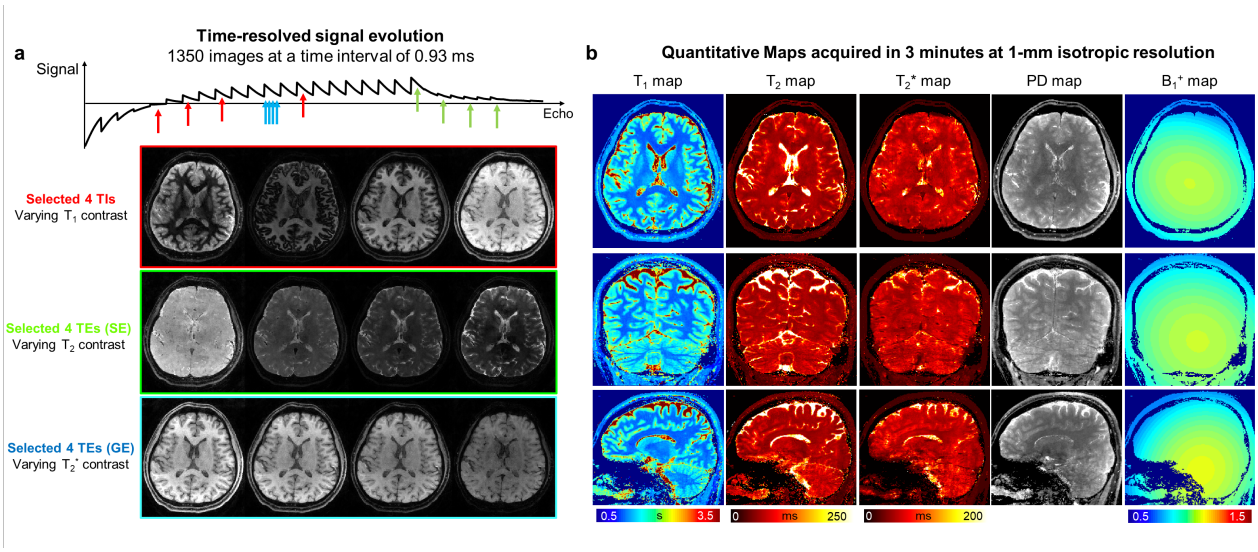


Figure 2. Simultaneous $T_1$, $T_2$ and $T_2^*$ mapping at 1-mm isotropic resolution whole-brain in 3 minutes acquired by 3D-EPTI. **a**, Representative reconstructed multi-contrast images with different $T_1$, $T_2$, and $T_2^*$ weightings selected from the 1350 resolved images. **b**, High-resolution quantitative maps estimated from the multi-contrast images, including $T_1$, $T_2$, $T_2^*$, PD and $B_1^+$, shown in three orthogonal views.

Conventionally, each of the three relaxation parameters is mapped sequentially, which requires lengthy acquisition time. To address this, many fast quantification methods have been developed recently to obtain $T_1$ and $T_2$[2,18,19,43-47], or $T_1$ and $T_2^*$[48-50] simultaneously, but there are only a limited number of approaches that target all of these three parameters simultanously[51-54]. Additionally, even by using these cutting-edge methods, whole-brain multi-parametric mapping at high isotropic resolution (e.g., 1-mm) can still take more than half an hour of acquisition time. To overcome this issue, 3D-EPTI aims to achieve ~10× faster acquisition than the state-of-the-art methods for simultaneous acquisition of $T_1$, $T_2$, and $T_2^*$. In addition to these quantitative parameters, 3D-EPTI also estimates the RF field inhomogeneity ($B_1^+$), a major confounding factor that affects the accuracy of

the measurement for relaxation times, therefore achieving high accuracy without the need of an additional calibration scan for $B_1^+$. Figure 2 demonstrates an example dataset acquired by 3D-EPTI at 1-mm isotropic resolution with whole brain coverage in just 3 minutes, resulting in a total of 1350 multi-contrast images resolved at a time interval as short as 0.93 ms (an echo-spacing). Representative reconstructed images with different $T_1$, $T_2$, $T_2^*$ contrasts illustrate the high quality in the reconstruction that can be achieved from a highly undersampled dataset by fully exploiting the intra- and inter-readout spatiotemporal correlations (Fig. 2a). The resultant quantitative parameter maps, PD and $B_1^+$ field show high image SNR and resolution, free from any image distortions or aliasing artifacts (Fig. 2b). These multi-parametric maps acquired in a single scan are also perfectly aligned without the need for co-registration. Moreover, the high isotropic resolution of these images allows them to be reformatted in any orientation without loss of resolution, improving the ability to visualize detailed structures and small lesions. The accuracy of the quantitative estimates, including $T_1$, $T_2$, $T_2^*$, PD and $B_1^+$, was also tested through a simulation study of the 3D-EPTI acquisition using gold standard reference parameter maps, where low errors were observed for all parameters as shown in Supplementary Fig. 2.

**Characterization of the repeatability and reliability for $T_1$, $T_2$, and $T_2$* mapping.**

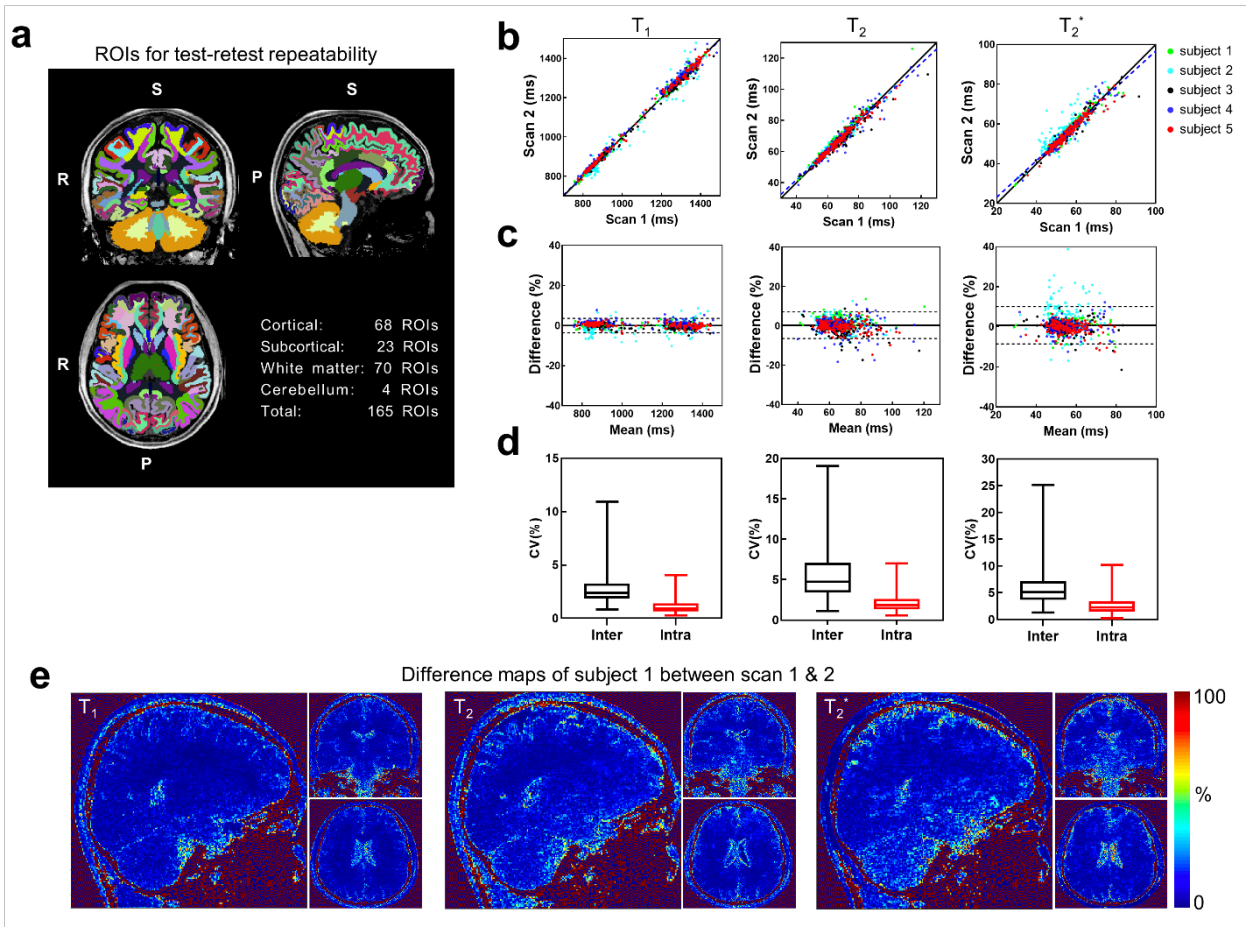


Figure 3. Repeatability test of 3D-EPTI for simultaneous $T_1$, $T_2$ and $T_2^*$ mapping using the 3-minute 1-mm protocol. **a**, 3D volumes are segmented into 165 ROIs covering the whole-brain area. **b**, Scatter plots of the test-retest $T_1$, $T_2$, $T_2^*$ values in the 165 ROIs measured from 5 subjects, shown along with the identity line (solid) and the regressed line (dashed). **c**, The Bland-Altman plot of the test-retest quantitative parameters. **d**, The box-plot of the coefficient of variation (COV) between

(inter) and within (intra) subjects. **e**, The percentage difference maps in subject 1 that shows the spatial distribution of the test-retest variation for the 3 parameters.

Quantitative repeatability is crucial for monitoring and characterization of brain tissues over time and among populations. To evaluate the repeatability of 3D-EPTI, a scan-rescan assessment was performed on 5 healthy volunteers using the 3-minute 1-mm protocol, where the subjects were taken out of the scanner and repositioned between the two scans. Region Of Interest (ROI) analysis was performed using automatic FreeSurfer[36,55,56] segmentation, which includes a total of 165 ROIs in cortical, subcortical, white matter and cerebellum regions after excluding cerebrospinal fluid (CSF) regions and ROIs smaller than 50 voxels (Fig. 3a). High correlations and small differences were measured between the two scans for all three parameters as shown in Fig. 2b and 2c. Specifically, the $T_1$ values from the first and the second scans are highly correlated with a positive Pearson's correlation coefficient (PCC) of 0.996 ($P < 0.0001$). Bland Altman analysis revealed no significant difference ($P = 0.821$, two-tailed *t*-test) between the two measurements. The $T_2$ values of the two scans show a high positive correlation (PCC = 0.974, $P < 0.0001$) with a small difference of 0.28% ($P = 0.017$), and the $T_2^*$ values also show a high positive correlation (PCC = 0.938, $P < 0.0001$) and a small difference of 0.80% ($P < 0.0001$). The scan-rescan difference maps (Fig. 3e) show a low level of differences and a relative homogeneous distribution in the gray and white matter areas of interest, while large differences are mainly observed in the CSF regions, which could be attributed to the high physiological noise in these regions.

The intra-subject variability between test-retest scans and inter-subject variability among the five volunteers were also evaluated and compared using coefficient of variation (COV). Figure 3d shows the distribution of the intra-subject and inter-subject COVs across all ROIs in box plots with whiskers from minimum to maximum data points. Small intra-subject variability was observed with a median COV at 0.93%, 1.88% and 2.27% for $T_1$, $T_2$ and $T_2^*$ respectively. The inter-subject COVs were also measured to be at a low level, with median COVs of 2.39%, 4.75%, 5.09%, which are higher than the intra-subject measurements as expected. The overall low level of COVs demonstrates the high level of repeatability of the 3D-EPTI quantifications, while the expected differences between intra- and inter-subject suggest the potential ability of 3D-EPTI in capturing individual differences. The $T_2^*$ values show the largest variability that could be reflective of the variability in the head position between the scan and rescan acquisitions, where previous findings have demonstrated variability in $T_2^*$ values as a function of head orientation relative to the main field[57]. The repeatability of $B_1^+$ mapping was also evaluated, where consistent measurements were obtained across three scans at different spatial resolutions for the same subject as shown in Supplementary Fig. 3.

To further validate 3D-EPTI's reliability, a comparison study between quantitative parameters provided by 3D-EPTI and those from lengthy standard acquisition methods was conducted *in vivo*. The well-established standard methods provide high quality quantitative parameters at a cost of impractically long acquisition time and therefore a higher level of susceptibility to motion induced artifacts. To mitigate this issue in our comparison, we reduced the spatial resolution ($2 \times 2 \times 3$ mm$^3$ for $T_1$ and $T_2$) as well as the slice coverage of the standard acquisitions to keep them to an acceptable total acquisition time of 53 minutes. For 3D-EPTI, a single 3-minute scan at 1-mm isotropic resolution with whole brain coverage was used to obtain all the quantitative estimates.

ROI analysis was performed with 14 manually selected ROIs that were contained within the slice coverage of standard 2D acquisitions as shown in Fig. 4. $T_1$ measurements of 3D-EPTI and the standard method show high positive correlation (PCC = 0.972, P < 0.0001), with a bias of -7.23% (P < 0.0001). Similarly, $T_2$ measurements also show high positive correlation (PCC = 0.790, P = 0.0008) with no significant bias (P = 0.1351). Lastly, $T_2^*$ values are also highly correlated (PCC = 0.948, p < 0.0001) with a small bias of 4.68% (P = 0.0137). In addition to the in-vivo validation, a phantom experiment was also performed where the quantitative measurements from 3D-EPTI are in good agreement with the standard methods (Supplementary Fig. 4).

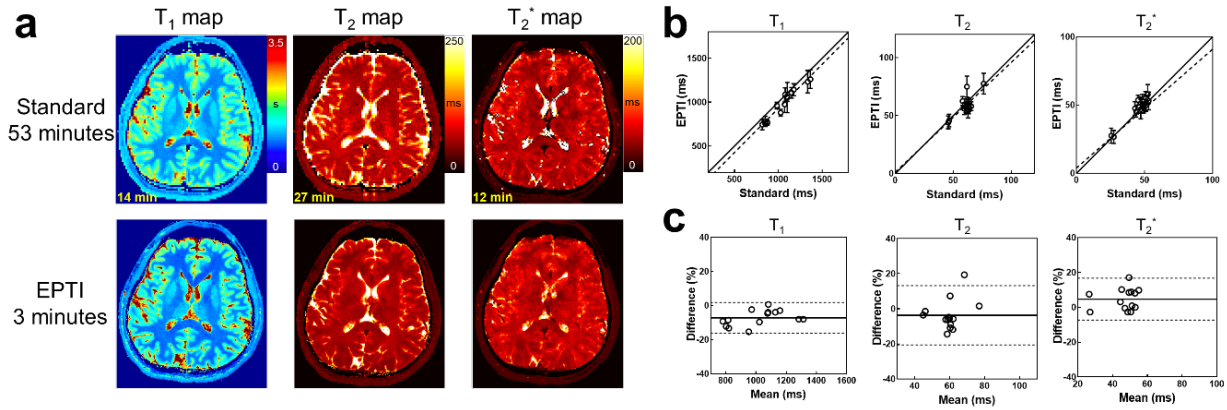


Figure 4. Comparison of the quantitative measurements obtained using 3D-EPTI vs. well-established but lengthy standard acquisitions *in vivo*. **a**, The quantitative maps acquired by the standard methods and 3D-EPTI. **b**, The scatter plots of the quantitative values from 14 selected ROIs. **c**, The Bland-Alman plot of the same data.

**Ultra-fast 1-min scan and submillimeter mapping enabled by the high efficiency.**

In addition to the 3-minute 3D-EPTI protocol at 1-mm isotropic resolution, two additional whole-brain protocols at different resolutions were developed with the purpose of showcasing the new possibilities that 3D-EPTI can bring and the unmet needs that it can address for multi-parametric imaging.

First, an ultra-fast 1-minute protocol at 1.5-mm isotropic resolution was developed to obtain high quality quantitative maps as shown in Fig. 5 and Supplementary Fig. 5. A one-minute ultra-fast scan has been an alluring target for the MRI research community, that would enable rapid screening exam and dramatically improve patient comfort and throughput. Recent studies have shown promising progress to acquire multi-contrast weighted images in 1 minute[58], but no study so far has been able to obtain quantitative parameters in a scan as short as 1 minute at a reasonable isotropic spatial resolution, let alone simultaneously mapping three quantitative parameters at once. The 1-minute multi-parametric scan provided by 3D-EPTI could help fulfill this important unmet need. The quick 3D-EPTI scan can also markedly reduce the chance of involuntary movements, a major source of image artifacts in MRI, particularly in less compliant clinical patients (e.g., pediatric patients), and reduce costly re-scan and patients called backs[59] as well as the need of harmful anesthesia[60].

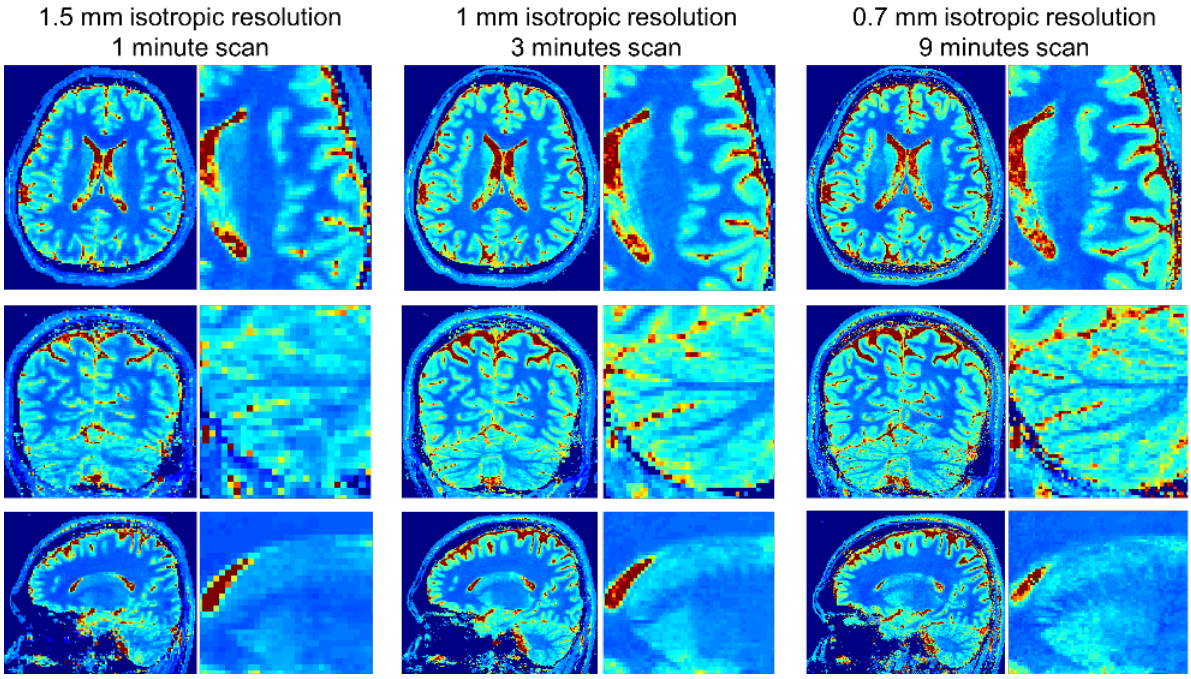


Figure 5. Example $T_1$ maps with zoomed-in areas provided by 3D-EPTI protocols at different spatial resolutions: 1-minute scan at 1.5-mm isotropic resolution, 3-minute scan at 1-mm isotropic resolution, and 9-minutes scan at 0.7-mm isotropic resolution.

Another protocol has also been developed for the acquisition of 0.7-mm isotropic resolution quantitative parameters in 9 minutes, to allows visualization and analysis of more detailed brain structures (Fig. 5, right column). This should be particularly helpful in studying the intra-cortical architecture of the human brain, where the thin cortex consists of multiple layers with different tissue properties, such as different levels of myelination or iron concentration. The use of quantitative methods has emerged recently for better evaluation of these different properties[61-67], but a lack of acquisition efficiency for high resolution imaging has been one of the key obstacles. The high efficiency of 3D-EPTI enables for the first-time simultaneous acquisition of $T_1$, $T_2$, $T_2^*$ at submillimeter resolution within a few minutes, and provides a new powerful tool to study cortical layer-dependent tissue properties. Importantly, this acquisition protocol has been designed for use on widely available clinical MRI instrumentations (3 Tesla MRI with 32-channel receiver array), where 3D-EPTI enables the ability to acquire high-quality sub-millimeters parameter maps with good SNR without need of specialized hardware (e.g., ultra-high-field scanner).

Here, we explored the feasibility of using 3D-EPTI to assess intra-cortical structures of healthy volunteers, evaluated its inter-scan and inter-subject repeatability, and explored its potential to identify specific spatial features. Figure 6a shows the quantitative maps of all three parameters at different cortical depth from inner (proximate to white matter) to outer (proximate to CSF) surface of a healthy volunteer. Consistent profiles across layers can be observed with distinctly lower values in areas that are highly myelinated, such as motor, sensory, auditory, MT and visual cortex, which are in accordance with previous literatures[61,64-66,68]. For all three relaxation parameters, there is a general increasing trend across cortical layers from inner to outer surface, potentially reflecting the decrease of myelin and iron contents from the white matter surface to the CSF surface

that has been validated in histological studies[69]. Figure 6b shows an example of such a profile within a representative ROI in the motor cortex (BA 4a), where consistent profiles from 4 healthy volunteers (color-coded) across two repeated scans (solid and dashed lines) were plotted, showing high inter-scan (intra-subject) and inter-subject repeatability. The high repeatability is also observed in all other representative ROIs as shown in Fig 6d and 6e, quantified by both the root mean square errors (RMSEs) and the PCC, which assess the differences and the similarities of the cortical profiles among subjects and between scans. The intra-subject profiles were measured with low differences (median RMSEs for $T_1$, $T_2$, $T_2^*$ at 20.36 ms, 1.84 ms and 2.94 ms) and high correlations (median PCCs at 0.999, 0.999,0.992). The inter-subject profiles showed higher variability than intra-subject as expected, but still with low median RMSEs at 38.47 ms, 4.37 ms and 4.42 ms as well as high median PCCs at 0.998, 0.995, 0.988 for $T_1$, $T_2$, $T_2^*$ respectively.

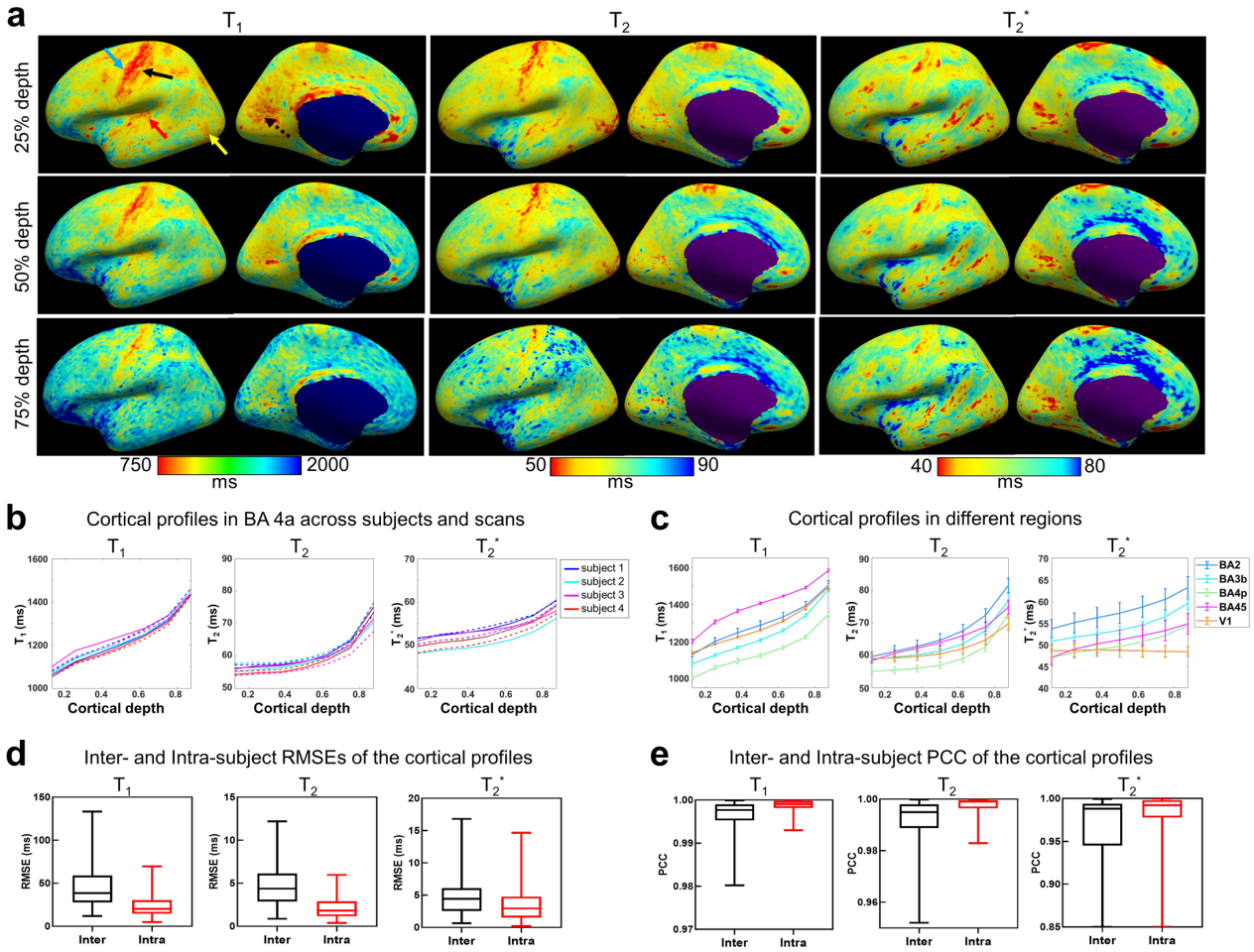


Figure 6. Surface-based cortical analysis of $T_1$, $T_2$ and $T_2^*$ of 0.7-mm isotropic resolution 3D-EPTI data. **a**, Quantitative parameters sampled at three different cortical depths (25%, 50%, 75%) shown on the reconstructed cortical surface. Lower quantitative values were observed in highly-myelinated regions such as motor (blue arrow), somatosensory (black arrow), auditory (red arrow), middle temporal visual area (yellow arrow) and visual cortex (dotted black arrow). **b**, Example of quantitative values as a function of cortical depth in the BA 4a area of 4 subjects across 2 repeated scans (solid line: scan 1, dashed line: scan 2). **c**, Averaged quantitative values over the 2 scans across 4 subjects as function of cortical depth in 5 representative ROIs. Error bars represent the standard deviations between the 4 subjects. **d**, Box plots of the root-mean-square-errors (RMSEs) of the cortical profiles of the quantitative parameters calculated between (inter) and within (intra) subjects. **e**, Box plots of Pearson correlation coefficients (PCCs) of the profiles calculated between (inter) and within (intra)

subjects.

Despite the remarkable consistency across scans and subjects, the cortical profiles differ across different cortical regions. The average profiles in Fig. 6c revealed different slopes and global values in different ROIs. The results provided by 3D-EPTI in a dramatically reduced scan time agree well with previous literatures investigating $T_1$ or $T_2^*$ cortical profiles[62,65,66]. For example, highly myelinated areas such as the motor (BA 4p), and the sensory (BA 3b) areas have globally lower $T_1$ profiles than other areas. A relative flat $T_2^*$ profile was observed in the visual cortex, which was also reported previously[65,66] and might be attributed to the highly myelinated middle layers and increasing susceptibility in the outer layers due to presence of blood vessels with a high level of iron. Previous studies investigating $T_2$ profiles across cortical depths have been lacking due to the need for prohibitively long acquisitions. Using 3D-EPTI, different $T_2$ profiles were also obtained in different ROIs, which could reflect differences in both myelin water content and iron composition and complement to the findings in $T_1$ and $T_2^*$.

**Generating arbitrary image contrasts with adjustable weightings**

Current clinical MRI relies on contrast-weighted images, which are acquired by sequentially applying multiple sequences with predetermined acquisition parameters. This is time consuming, requires cross-contrast registration, and results in suboptimal contrast if there are substantial individual differences, particularly in the case of abnormalities. In a single scan within minutes, 3D-EPTI not only provides co-registered simultaneous quantitative maps as mentioned above but is also able to generate arbitrary image contrasts with adjustable contrast weightings, yielding optimized visualization for the tissue or lesion of interest. Figure 7 demonstrated the contrast-synthesizing ability of 3D-EPTI in several examples. First, the standard routine clinical contrasts, MPRAGE, $T_2$-FLAIR and $T_2$-weighted, were synthesized with high quality for all of the three protocols (Fig. 7a). Double inversion recovery (DIR) was also generated as an example to provide superior cortical visualization. Previously, despite its higher sensitivity in the detection of cortical lesions for multiple sclerosis[70,71], the adoption of DIR to clinical applications has been limited by the low SNR and lengthy acquisition. With 3D-EPTI, DIR or any other useful contrasts can be synthesized simultaneously after a few minutes of scan. The isotropic resolution of the 3D-EPTI protocols also facilitate the flexibility of viewing the images in arbitrary orientations (Fig.7b). Moreover, the weighting of each of these contrasts is adjustable to provide optimal visualization without the need to re-scan the subject. For instance, the contrast-determining parameters of an IR-SE sequence (FLAIR), TI and TE, can be freely adjusted across a wide range, resulting in a spectrum of possible contrasts between white and gray matter (Fig. 7c). From the spectrum, a particular set of parameters can be identified and selected for final image synthesis, such as the ones that offer the maximum white-grey contrast. We also showed the maximum image contrast between CSF and gray matter using a different set of parameters identified from their spectrum. Here, the CSF, gray and whitter matter were used as an illustration of the contrast optimization framework in healthy volunteer, but this can be easily applied to any tissue or lesion types to improve the diagnostic power of MRI.

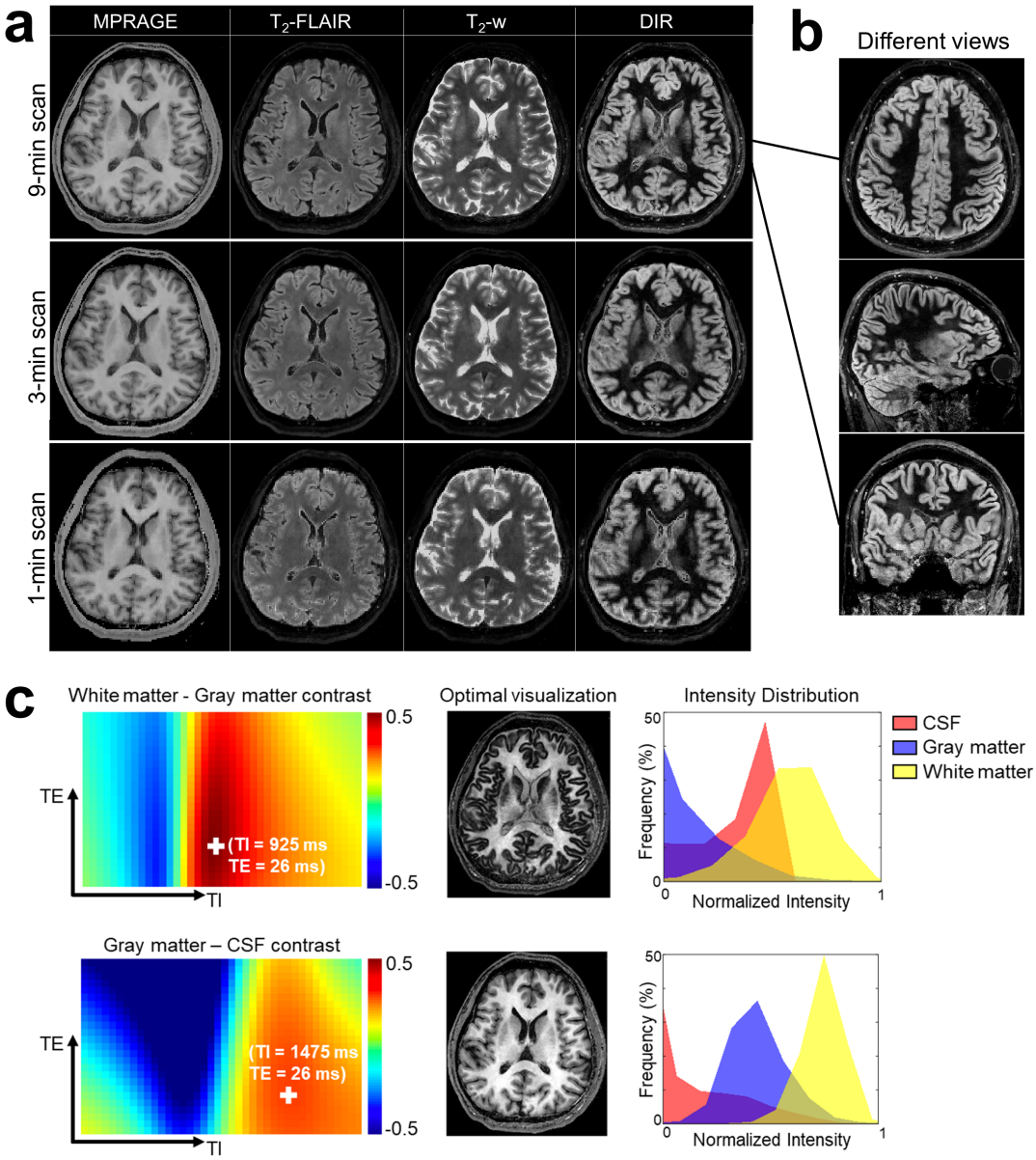


Figure 7. Synthesized multi-contrast images using 3D-EPTI. **a**, Synthetic MRRAGE, $T_2$-FLAIR, $T_2$-weighted, and double-inversion recovery (DIR) contrasts from three protocols (9-min 0.7-mm protocol, 3-min 1-mm protocol, and 1-min 1.5-mm protocol). **b**, Example of the flexibility in visualization in different views of the synthesized images at high isotropic resolution. **c**, Example of contrast-optimized visualization between target-tissue pair by adjusting sequence parameters (TI and TE). Two examples that maximized the contrast differences i) between white matter and gray matter, and ii) between gray matter and CSF, are presented. The spectrum of contrast difference between the two tissues (c, left panel) is used to select the parameters to synthesize the contrast for optimal visualization (c, middle panel). The intensity distribution of the optimized contrast in three tissues are shown at the right panel.

## 3. Discussion

The goal of this study is to address the long-standing problem in quantitative MRI — the slow acquisition speed. The key concept in 3D-EPTI of exploiting spatiotemporal correlation at multiple timescales through new encoding strategies within and between its efficient continuous readouts was used to achieve rapid quantitative

MRI. This has allowed the acquisition of robust multi-parametric maps within minutes at high isotropic resolution with whole brain coverage. As a proof-of-concept, a 3D-EPTI sequence for simultaneous $T_1$, $T_2$ and $T_2^*$ mapping was developed and validated, as these are the fundamental relaxation time constants that determine the contrast of most MR images.

High intra-subject repeatability of the quantitative parameters obtained using 3D-EPTI was demonstrated across multiple healthy volunteers. This will be critical to the success of future deployment of 3D-PTI to various applications such as in longitudinal monitoring of healthy and diseased tissues during complex biological process of brain development or pathophysiological progression of neurological diseases. Nonetheless, despite our efforts to minimize the bias in the repeatability assessment process itself, such as by using automatically segmented ROIs instead of manual ROIs, the small variations (bias < 0.8% and COV < 2.27%) could still be partially caused by errors in the registration process to align the two scans for comparison. Moreover, inherent differences between scans are possible. For example, $T_2^*$ shows slightly higher variability than $T_1$ and $T_2$, which may be explained by the differences due to its dependence on head orientations relative to the main magnetic field.

The high inter-subject repeatability (COV < 5.09%) of the quantitative parameters obtained using 3D-EPTI on healthy volunteers points to its potential for use in establishing population-average norms or atlases. Currently, multi-parametric MRI atlases are still lacking, but the short scans enabled by 3D-EPTI can significantly improve the cost effectiveness and facilitate large-scale studies for this purpose. On the other hand, as expected, the inter-subject repeatability is lower than the intra-subject repeatability. This could reflect the ability of 3D-EPTI to detect inherent individual differences, pointing to its potential in providing sensitive quantitative biomarkers. However, some of the increased variability could also be attributed to the additional segmentation variabilities across subjects, especially in challenging areas such as the optic chiasm. High intra- and inter-subject repeatability was also observed in the intra-cortical profiles obtained by 3D-EPTI. This illustrates the robust performance in using 3D-EPTI data to conduct reliable surface reconstruction and reveal repeatable subtle features across cortical layers. In addition to its potential for use in longitudinal monitoring and in establishing quantitative biomarkers, 3D-EPTI could be used to evaluate spatially varying profiles of cortical myelination and iron concentration.

The reliability of the quantitative measures obtained using 3D-EPTI was further validated by comparing them to ones obtained using lengthy standard acquisitions, where a generally high level of agreement was observed in both in-vivo (Fig. 4) and phantom (Supplementary Fig. 4) experiments. The largest difference was observed in the in-vivo $T_1$-values, with a bias level of 7.23%. This could potentially be attributed to the magnetic transfer (MT) effect, which causes a different level of exchange between water and macromolecular pools in different sequences. This can create discrepancies between the actual and the modelled signal evolutions in both 3D-EPTI and in the standard acquisition, where the MT effect has not been accounted for. Such an effect is more prominent in $T_1$ quantification, due to the use of an inversion recovery pulse. The characterization and disentanglement of the MT effect in quantitative mapping is an active area of research[72]. Future work will investigate the incorporation of a MT-sensitive sequence module into the 3D-EPTI acquisition, and model the

MT effect in both the reconstruction and parameter fitting.

With its unprecedented high efficiency for simultaneous multi-parametric mapping at high resolution with high repeatability, 3D-EPTI has the potential to enable the next-generation of brain examination. In such an examination, after 'one click', multiple quantitative parameters can be acquired in a single fast scan within a few minutes at high resolution and whole brain coverage. Images with the optimal contrasts of choice can then be generated post-acquisition and visualized in arbitrary views. Moreover, with robust quantitative measures, abnormal changes can be automatically detected by comparing with established norms, and further monitored over time. Beyond traditional diagnosis, the accuracy of computer-assisted diagnostic algorithms particularly with machine learning can also benefit from the adoption of quantitative imaging data, where standardized data with high repeatability will enable better network training. The successful implementation of these technologies should facilitate a more efficient, accurate and cost-effective diagnostic work-flow, and provide a powerful tool for neuroscientific research.

The concept of 3D-EPTI can be readily adopted to other pulse sequences for the quantification of other tissue parameters. For example, 3D-EPTI should be exceptionally well suited for parameters estimation for multiple pools models, because it can continuously track complex signal evolution at a very short time scale (< 1 ms) to offer more degrees of freedom in estimating these parameters. The concurrent distortion- and blurring-free multi-contrast images obtained with 3D-EPTI can also be used in combination with the quantitative parameters. A simple example is the adoption of this work into a typical functional MRI sequence, where the obtained $T_2^*$ value can be used to optimally combine time-resolved multi-echo images to enhance the contrast-to-noise ratio. The unique features of 3D-EPTI also open up many possibilities for further technical improvements. For example, the radial-block sampling of 3D-EPTI grants it the ability to monitor and correct subject movements between repetitions for motion-immune scanning. Other advanced reconstruction algorithms, including machine learning and multi-dimensional low-rank tensor approach, may further improve the accuracy of time-resolving reconstruction.

## 4. Methods

### Pulse sequence and encoding design

IR-GE and VFA-GRASE[27] sequences were implemented to provide high sensitivity to $T_1$, $T_2$, and $T_2^*$, with the continuous 3D-EPTI readout inserted after each excitation (i.e., each TI or SE) (Fig. 1a). In the IR-GE sequence, an adiabatic inversion pulse was applied, followed by 20 excitation pulses with small flip angles (30°). In the VFA-GRASE sequence, 10 variable-flip-angle refocusing pulses were applied after the 90° pulse with flip angles of 122°, 58°, 44°, 41°, 41°, 46°, 158°, 189°, 43°, 30°. The flip angles and the timing of the pulse sequence were chosen based on the results of an optimization considering both the signal amplitude and the differentiability between tissues. All the excitation and refocusing RF pulses in the IR-GE and GRASE sequences were non-selective with short pulse durations (0.5 ms for excitation and 1 ms for refocusing), therefore resulting in shorter achievable starting echo time and shorter sampling interval. Readout gradient was

applied along the Head-Foot (HF) direction to avoid signal wrap from the non-selective excitation. Spectrally-selective fat saturation was applied before each excitation pulse in the IR-GE sequence and before the 90° pulse in the GRASE sequence. Spoiling gradients were applied after each readout in the IR-GE sequence, and crusher gradients were used for each refocusing pulse in the GRASE sequence.

The 3D-EPTI acquisition was performed to encode data in a 4D spatiotemporal space (*k-t* space) to capture the signal temporal evolution across the readouts in the IR-GE and VFA-GRASE sequences. The frequency space (*k*-space) itself consists of three encoding dimensions, $k_x$, $k_y$, and $k_z$, where $k_x$ is the so-called frequency encoding, and $k_y$ and $k_z$ are the two phase-encoding dimensions. To achieve efficient encoding and fast scan, a number of tailored undersampling strategies were carefully designed and synergistically employed within and across the 3D-EPTI readouts. In each 3D-EPTI readout, a block of *k-t* space ($k_y$-$k_z$-$t$) is acquired, which contains multiple time segments of "echo sections" (Supplementary Fig. 6). In each echo section, the $k_y$-$k_z$ sampling locations at different time points are arranged to be complementary and are acquired in an interleaved fashion using a spatiotemporal controlled aliasing sampling strategy[73]. The distance between $k_y$-$k_z$ samples within each echo section was kept within the capability of parallel imaging and coil sensitivity to recover the missing points. The distance along time was kept to 6-8 ms by using a small block size. Within each readout, two complementary CAIPI pattern were used across echo sections to provide additional independent sampling that has been shown to further improve the reconstruction performance at high acceleration rates[28]. The encoding patterns used in the 1.5-mm/1-mm protocol and 0.7 mm protocol are illustrated in Supplementary Fig. 6. For each 3D-EPTI readout, the overall acceleration factor in *k-t* space is equal to the block size ($k_y \times k_z$), as only one data point is sampled at each time point in the block. An acceleration factor of 80 ($k_y \times k_z = 8 \times 10$) was utilized for 1.5-mm and 1-mm acquisitions, while a smaller acceleration factor of 48 ($k_y \times k_z = 8 \times 6$) was used for the 0.7-mm acquisition to compensate for the larger time interval (larger echo spacing).

In each TR of the IR-GE and VFA-GRASE sequences, one $k_y \times k_z$ block is acquired in each of the readout. To quickly encode the 4D *k-t* space using a small number of TRs, a golden-angle radial block sampling is employed across the readouts (Supplementary Fig. 6). Different blocks are acquired at different TRs to compose a block-wise golden-angle radial pattern at every TI and SE, with the radial pattern rotating with a golden angle across the different readouts. Such radial sampling creates spatiotemporal incoherent aliasing that is well suited for constrained subspace reconstruction. It provides additional acceleration on top of the acceleration within the block, where the acceleration factor depends on how many lines of radial blocks are acquired. The detailed design of radial-block sampling is shown in Supplementary Fig. 7. For the 1-mm protocol, 2 radial lines were acquired for the IR-GE sequence in 45 TRs (instead of 23×23=529 TRs without radial-block acceleration), and 3 radial lines in 65 TRs were acquired for the GRASE sequence. More lines were acquired in GRASE to compensate for the fewer number of readouts to encode the *k-t* space (10 SEs in GRASE vs. 20 TIs in IR-GE). For the 1.5-mm protocol, 3 radial lines with a reduction factor of 2 along the radial direction, equivalent to 1.5 lines, were acquired in 23 TRs (instead of 15×15=225 TRs), and 2 radial lines were acquired for GRASE in 29 TRs. The 0.7-mm protocol acquired 4 radial lines for both IR-GE and GRASE in a total of 161 TRs (instead of 41×41=1681 TRs) to provide sufficient sampling for higher spatial resolution.

## Image Reconstruction

The low-rank subspace method[22,28] was utilized to jointly reconstruct the IR-GE and VFA-GRASE multi-contrast images across different time points (Supplementary Fig. 1). At first, a large number of temporal signal evolutions were simulated using the Extended Phase Graphs (EPG) approach, each contains $N_t$ time points. A wide range of quantitative parameters were used to exhaust all possibilities of interest: $T_1$ from 400 ms to 5000 ms, $T_2$ from 10 ms to 500 ms, $T_2^*$ from 10 ms to 500 ms, $B_1^+$ factor from 0.75 to 1.25. Additional constraint of $T_2^*$ was also enforced to keep its value no higher than $T_2$. Second, $N_b$ subspace basis vectors $\phi \in \mathbb{C}^{N_t \times N_b}$ were extracted from these simulated signals by using principal component analysis (PCA). In this study, we selected 12 bases that can approximate the simulated signals with an error smaller than 0.2%. Then, the full time series of $N_v$ spatial voxels can be represented by $\phi c$, where $c \in \mathbb{C}^{N_b \times N_v}$ contains the coefficient maps of the subspace bases that can be estimated by solving:

$$\min_c \|UFSP\phi c - y\|_2^2 + \lambda R(c) \tag{1}$$

where $P \in \mathbb{C}^{N_v \times N_t}$ contains the phase evolutions across the time-series images including the background and $B_0$ inhomogeneity-induced phases, $S \in \mathbb{C}^{N_v \times N_c}$ denotes the coil sensitivity of a $N_c$-channel receiver coil, $F$ is the Fourier transform operator applied across the spatial dimensions, $U$ is the undersampling mask, and $y$ represents the acquired $k$-space data. The phase map $P$ and sensitivity map $S$ can be obtained from a low-resolution calibration pre-scan. A locally low-rank (LLR) regularization $R(c)$ was applied on coefficient maps with a control parameter $\lambda$ to further improve the conditioning. Since the number of unknowns in the optimization problem is significantly reduced from thousands of images to a few coefficient maps, the subspace method can achieve accurate image reconstruction for 3D-EPTI at high accelerations.

The subspace reconstruction was solved by the alternating direction method of multipliers (ADMM) algorithm[74] implemented in the Berkeley Advanced Reconstruction Toolbox (BART)[75,76]. A maximum number of iterations = 100 was set to be the stop criterion. Other parameters of the reconstruction including rho of ADMM and $\lambda$ of LLR were set at 0.01 and $3 \times 10^{-4}$ respectively. These reconstruction parameters were selected empirically based on the results of a simulation test (example simulation results shown in Supplementary Fig. 2). Each readout slice of the 3D volumetric dataset was reconstructed independently by applying the inverse Fourier Transform along the fully-sampled frequency-encoding direction before the reconstruction. After reconstruction, the quantitative parameters were estimated from a dictionary-based matching. The dictionary was generated using the EPG approach with the same parameter range used in the basis generation. After dictionary matching, the estimated $B_1^+$ maps were fitted by a 2nd-order polynomial function in the 3D spatial domain, with an assumption that $B_1^+$ fields vary smoothly in the spatial domain, which were then fed back into the dictionary matching to obtain more accurate quantitative parameters.

## Acquisition parameters

All data were acquired on a Siemens Prisma 3T scanner with a 32-channel head coil (Siemens Healthineers,

Erlangen, Germany). The 3D-EPTI protocols were used in the scan-rescan experiment where the subject was taken out of the scanner and repositioned between the two scans.

The 1-mm 3D EPTI data were all acquired with the following parameters: FOV = 220 × 176 × 210 $mm^3$ (AP-LR-HF), matrix size = 230 × 184 × 210, spatial resolution = 0.96 × 0.96 × 1 $mm^3$, echo spacing = 0.93 ms, TR of IR-GE = 2600 ms, TR of GRASE = 800 ms. There were 20 readouts in IR-GE, each containing 48 echoes, and 10 readouts in GRASE, each containing 39 echoes. The total acquisition time was ~3 minutes, including 117 seconds for IR-GE, 54 seconds for GRASE, and a 12-second calibration scan. The *k-t* calibration scan was acquired to estimate the $B_0$ and coil sensitivity maps using a GE sequence with bipolar readouts, where data were acquired with the same FOV and echo spacing as the imaging scan. Other relevant acquisition parameters were: matrix size = 42 × 32 × 210, number of echoes = 9, TR = 24 ms. The *k*-space center (8 × 8) was fully-sampled and the rest of *k*-space was undersampled along $k_y$ and $k_z$ by a factor of 2 × 2. GRAPPA[16] was used to reconstruct the missing data points in the calibration data. The calibration scan for all of the following acquisitions used the same matrix size along $k_y$ and $k_z$ with the same acceleration factor.

The acquisition parameters for the 1.5-mm protocol were: FOV = 218 × 173 × 230 $mm^3$ (AP-LR-HF), matrix size = 150 × 120 × 154, spatial resolution = 1.45 × 1.44 × 1.49 $mm^3$, TR of IR-GE = 1900 ms, TR of GRASE = 600 ms, echo spacing = 0.72 ms, each readout contained 53 echoes in IR-GE, and 39 echoes in GRASE. The total acquisition time was ~ 1 minute, including 44 s for IR-GE and 17 s for GRASE. The 1.5-mm calibration scan took 10 seconds with a TR = 20 ms.

The acquisition parameters for the 0.7-mm protocol were: FOV = 224 × 176.4 × 224 $mm^3$ (AP-LR-HF), matrix size = 328 × 246 × 322, spatial resolution = 0.68 × 0.72 × 0.70 $mm^3$, TR of IR-GE = 2600 ms, TR of GRASE = 800 ms, echo spacing = 1.2 ms, each readout contained 42 echoes in IR-GE, and 33 echoes in GRASE. The total acquisition time was ~ 9 minutes, including 7 min for IR-GE and 2 min for GRASE. The calibration scan took 12 seconds with 7 echoes and a TR of 24 ms.

To obtain reference quantitative maps for comparison, conventional gold-standard acquisition approaches were used, including 2D IR-SE for $T_1$ mapping, 2D single-echo SE for $T_2$ mapping, and 3D multi-echo GRE for $T_2^*$ mapping. In the phantom experiment, the acquisition parameters of the IR-SE sequence for $T_1$ mapping were: FOV = 256 × 256 $mm^2$, in-plane resolution = 1 × 1 $mm^2$, slice thickness = 3 mm, number of slices = 9, acceleration factor along $k_y$ = 2, TR = 8000 ms, TIs = 100, 200, 400, 800, 1600, 3200 ms. The $T_2$ mapping was performed using the single-echo SE sequence with the same FOV, resolution, and acceleration as in IR-SE. The TR was 3000 ms, and 6 echo times (25, 50, 75, 100, 150, 200 ms) were acquired to achieve robust fitting. The 3D multi-echo GRE sequence was used for the $T_2^*$ mapping with FOV = 186 × 176 × 224 $mm^3$ at 1-mm isotropic resolution. Seven echo times (5, 10, 15, 25, 35, 45, 60 ms) were acquired with an acceleration factor of 2 × 2 ($k_y \times k_z$). The total acquisition time for the phantom reference scans was about 1.5 hours, including 30 minutes for IR-GE, 50 minutes for single-echo SE, and 12 minutes for 3D GRE. The same sequences were used for the in-vivo test, however, a lower resolution of 2 × 2 $mm^2$ was used in the IR-SE and single-echo SE sequences to reduce the scan time and mitigate potential motion-induced artifacts. Most of the other parameters were kept the same as the phantom scan, except for, the number of slices = 19 for IR-SE and single-echo SE, TEs of single-

echo SE = 25, 50, 75, 100, 140, 180 ms, a higher acceleration factor along $k_y = 3$ for IR-GE and single-echo SE, and FOV of 3D-GRE = 216 × 176 × 210 $mm^3$. Even with the lower resolution and higher acceleration, the total scan time was still about 53 minutes, including 27 minutes for single-echo SE, 14 minutes for IR-SE, and 12 minutes for GRE.

**Image processing and analysis**

In the test-retest experiment, the quantitative maps from the two scans were first registered using FLIRT[77-79]. Then, the average $R_1$ maps of each subject were used for Freesurfer segmentation, which resulted in 165 ROIs in cortical, subcortical, white matter and cerebellum regions after removing CSF regions and ROIs smaller than 50 voxels. For cortical analysis, surface-based cortical reconstruction was performed using Freesurfer[36,55,56] on the $R_1$ maps separately for each subject and for each scan. 9 equi-volume[62,80] cortical layers were reconstructed, and applied to all quantitative maps to investigate their distribution across different cortical depths. These maps were sampled onto the average subject space with a 2-mm Gaussian surface smoothing for final analysis.

Synthetic images are synthesized from the calculated quantitative maps based on signal equations of the specific sequences. To illustrate the contrast optimization framework (Fig. 7c), a spectrum of the contrast difference between two tissues was obtained using a range of acquisition parameters. The mean value of the synthesized image intensity of the target tissues was used to calculate the contrast difference. The tissue can be identified by the acquired quantitative maps, for example, a threshold-hold based segmentation on $T_1$ map was performed in this instance to generate masks for gray matter, white matter and CSF.

**Materials**

All of the reconstructions were performed in MATLAB using a Linux workstation (CPU: Intel Xeon, 3.00GHz, 24 Cores; RAM: 512 GB; GPU: Quadro RTX 5000, 16 GB memory). The reconstruction time for each imaging slice in the 1-mm dataset was about 1 minute, and the reconstruction of the whole-volume took about 3 hours using one GPU.

**Human subjects**

Informed consent was collected from all healthy volunteers before imaging, with an institutionally approved protocol.

## Acknowledgments

This work was supported by NIH NIBIB (R01-EB020613, R01-EB019437, R01-MH116173, P41-EB030006 and U01-EB025162) and by the MGH/HST Athinoula A. Martinos Center for Biomedical Imaging; and was made possible by the resources provided by NIH Shared Instrumentation Grants S10-RR023401, S10-RR023043, and S10-RR019307. We also thank Dr. Gliad Liberman's help on the GPU implementation of the image reconstruction.

## References


1. Tofts, P. *Quantitative MRI of the brain: measuring changes caused by disease*. (John Wiley & Sons, 2005).
2. Ma, D. *et al.* Development of high-resolution 3D MR fingerprinting for detection and characterization of epileptic lesions. *J. Magn. Reson. Imaging* **49**, 1333-1346 (2018).
3. Bernasconi, N. *et al.* Entorhinal cortex in temporal lobe epilepsy: a quantitative MRI study. *Neurology* **52**, 1870-1870 (1999).
4. Lescher, S. *et al.* Quantitative T1 and T2 mapping in recurrent glioblastomas under bevacizumab: earlier detection of tumor progression compared to conventional MRI. *Neuroradiology* **57**, 11-20 (2015).
5. Müller, A. *et al.* Quantitative T1-mapping detects cloudy-enhancing tumor compartments predicting outcome of patients with glioblastoma. *Cancer med.* **6**, 89-99 (2017).
6. Tardif, C. L., Bedell, B. J., Eskildsen, S. F., Collins, D. L. & Pike. G. B. Quantitative magnetic resonance imaging of cortical multiple sclerosis pathology. *Mult. Scler. Int.* **2012** (2011).
7. West, J. *et al.* Normal appearing and diffusely abnormal white matter in patients with multiple sclerosis assessed with quantitative MR. *PloS one* **9**, e95161 (2014).
8. Reitz, S. C. *et al.* Multi-parametric quantitative MRI of normal appearing white matter in multiple sclerosis, and the effect of disease activity on T2. *Brain Imaging Behav.* **11**, 744-753 (2017).
9. Ramani, A., Jensen, J. H. & Helpern, J. A. Quantitative MR imaging in Alzheimer disease. *Radiology* **241**, 26-44 (2006).
10. Falangola, M. *et al.* Quantitative MRI reveals aging-associated T2 changes in mouse models of Alzheimer's disease. *NMR Biomed.* **20**, 343-351 (2007).
11. Sled, J. G. & Nossin-Manor, R. Quantitative MRI for studying neonatal brain development. *Neuroradiology* **55**, 97-104 (2013).
12. Bozzali, M., Serra, L. & Cercignani, M. Quantitative MRI to understand Alzheimer's disease pathophysiology. *Curr. Opin. Neurol.* **29**, 437-444 (2016).
13. Filo, S. *et al.* Disentangling molecular alterations from water-content changes in the aging human brain using quantitative MRI. *Nat. Commun.* **10**, 1-16 (2019).
14. Sodickson, D. K. & Manning, W. J. Simultaneous acquisition of spatial harmonics (SMASH): Fast imaging with radiofrequency coil arrays. *Magn. Reson. Med.* **38**, 591-603 (1997).
15. Pruessmann, K. P., Weiger, M., Scheidegger, M. B. & Boesiger, P. SENSE: sensitivity encoding for fast MRI. *Magn. Reson. Med.* **42**, 952-962 (1999).
16. Griswold, M. A. *et al.* Generalized autocalibrating partially parallel acquisitions (GRAPPA). *Magn. Reson. Med.* **47**, 1202-1210 (2002).
17. Lustig, M., Donoho, D. & Pauly, J. M. Sparse MRI: The application of compressed sensing for rapid MR imaging. *Magn. Reson. Med.* **58**, 1182-1195 (2007).
18. Ma, D. *et al.* Magnetic resonance fingerprinting. *Nature* **495**, 187-192 (2013).
19. Jiang, Y., Ma, D., Seiberlich, N., Gulani, V. & Griswold, M. A. MR fingerprinting using fast imaging with steady state precession (FISP) with spiral readout. *Magn. Reson. Med.* **74**, 1621-1631 (2015).
20. Cloos, M. A. *et al.* Multiparametric imaging with heterogeneous radiofrequency fields. *Nat. Commun.* **7**, 1-10 (2016).
21. Christodoulou, A. G. *et al.* Magnetic resonance multitasking for motion-resolved quantitative cardiovascular imaging. *Nat. Biomed. Eng.* **2**, 215-226 (2018).
22. Liang, Z.-P. Spatiotemporal imagingwith partially separable functions. In Proc. 4th IEEE Int. Symp. Biomed. Imaging 988-991 (IEEE, 2007).
23. Zhao, B. *et al.* Improved magnetic resonance fingerprinting reconstruction with low-rank and subspace modeling. *Magn. Reson. Med.* **79**, 933-942 (2018).
24. Mansfield, P. Multi-planar image formation using NMR spin echoes. *J. Phys. C Solid State Phys.* **10**, L55 (1977).
25. Breuer, F. A. *et al.* Controlled aliasing in volumetric parallel imaging (2D CAIPIRINHA). *Magn. Reson. Med.* **55**, 549-556 (2006).
26. Breuer, F. A. *et al.* Controlled aliasing in parallel imaging results in higher acceleration (CAIPIRINHA) for multi-slice imaging. *Magn. Reson. Med.* **53**, 684-691 (2005).
27. Oshio, K. & Feinberg, D. A. GRASE (gradient-and spin-echo) imaging: a novel fast MRI technique. *Magn. Reson. Med.* **20**, 344-349 (1991).

28. Dong, Z., Wang, F., Reese, T. G., Bilgic, B. & Setsompop, K. Echo planar time-resolved imaging with subspace reconstruction and optimized spatiotemporal encoding. *Magn. Reson. Med.* **84**, 2442-2455 (2020).
29. Guo, R. *et al.* Simultaneous QSM and metabolic imaging of the brain using SPICE: Further improvements in data acquisition and processing. *Magn. Reson. Med.* **85**, 970-977 (2021).
30. He, J. *et al.* Accelerated High-Dimensional MR Imaging With Sparse Sampling Using Low-Rank Tensors. *IEEE Trans. Med. Imaging* **35**, 2119-2129 (2016).
31. Zhao, B. *et al.* Accelerated MR parameter mapping with low-rank and sparsity constraints. *Magn. Reson. Med.* **74**, 489-498 (2015).
32. Lam, F. & Liang, Z. P. A subspace approach to high-resolution spectroscopic imaging. *Magn. Reson. Med.* **71**, 1349-1357 (2014).
33. Tamir, J. I. *et al.* T2 shuffling: sharp, multicontrast, volumetric fast spin-echo imaging. *Magn. Reson. Med.* **77**, 180-195 (2017).
34. Stüber, C. *et al.* Myelin and iron concentration in the human brain: a quantitative study of MRI contrast. *NeuroImage* **93**, 95-106 (2014).
35. Harkins, K. D. *et al.* The microstructural correlates of T1 in white matter. *Magn. Reson. Med.* **75**, 1341-1345 (2016).
36. Fischl, B. *et al.* Whole brain segmentation: automated labeling of neuroanatomical structures in the human brain. *Neuron* **33**, 341-355 (2002).
37. Odrobina, E. E., Lam, T. Y., Pun, T., Midha, R. & Stanisz, G. J. MR properties of excised neural tissue following experimentally induced demyelination. *NMR Biomed.* **18**, 277-284 (2005).
38. Gerlach, M., Ben-Shachar, D., Riederer, P. & Youdim, M. Altered brain metabolism of iron as a cause of neurodegenerative diseases? *J. Neurochem.* **63**, 793-807 (1994).
39. Chen, J. C. *et al.* MR of human postmortem brain tissue: correlative study between T2 and assays of iron and ferritin in Parkinson and Huntington disease. *Am. J. Neuroradiol.* **14**, 275-281 (1993).
40. Connor, J., Snyder, B., Beard, J., Fine, R. & Mufson, E. Regional distribution of iron and iron-regulatory proteins in the brain in aging and Alzheimer's disease. *J. Neurosci. Res.* **31**, 327-335 (1992).
41. Webb, S., Munro, C. A., Midha, R. & Stanisz, G. J. Is multicomponent T2 a good measure of myelin content in peripheral nerve? *Magn. Reson. Med.* **49**, 638-645 (2003).
42. Stanisz, G. J., Webb, S., Munro, C. A., Pun, T. & Midha, R. MR properties of excised neural tissue following experimentally induced inflammation. *Magn. Reson. Med.* **51**, 473-479 (2004).
43. Ma, S. *et al.* Three-dimensional simultaneous brain T1, T2, and ADC mapping with MR Multitasking. *Magn. Reson. Med.* **84**, 72-88 (2020).
44. Ma, S. *et al.* Three-dimensional whole-brain simultaneous T1, T2, and T1ρ quantification using MR Multitasking: Method and initial clinical experience in tissue characterization of multiple sclerosis. *Magn. Reson. Med.* **85**, 1938– 1952 (2021).
45. Fujita, S. *et al.* Three-dimensional high-resolution simultaneous quantitative mapping of the whole brain with 3D-QALAS: an accuracy and repeatability study. *Magn. Reson. Imaging* **63**, 235-243 (2019).
46. Warntjes, J., Leinhard, O. D., West, J. & Lundberg, P. Rapid magnetic resonance quantification on the brain: optimization for clinical usage. *Magn. Reson. Med.* **60**, 320-329 (2008).
47. Deoni, S. C., Rutt, B. K. & Peters, T. M. Rapid combined T1 and T2 mapping using gradient recalled acquisition in the steady state. *Magn. Reson. Med.* **49**, 515-526 (2003).
48. Metere, R., Kober, T., Möller, H. E. & Schäfer, A. Simultaneous quantitative MRI mapping of T1, T2* and magnetic susceptibility with multi-echo MP2RAGE. *PloS one* **12**, e0169265 (2017).
49. Caan, M. W. *et al.* MP2RAGEME: T1, T2*, and QSM mapping in one sequence at 7 tesla. *Hum. Brain Mapp.* **40**, 1786-1798 (2019).
50. Warntjes, J., Dahlqvist, O. & Lundberg, P. Novel method for rapid, simultaneous T1, T* 2, and proton density quantification. *Magn. Reson. Med.* **57**, 528-537 (2007).
51. Boyacioglu, R. *et al.* 3D magnetic resonance fingerprinting with quadratic RF phase. *Magn. Reson. Med.* **85**, 2084-2094 (2021).
52. Hong, T., Han, D. & Kim, D. H. Simultaneous estimation of PD, T1, T2, T2*, and$\Delta$ B0 using magnetic resonance fingerprinting with background gradient compensation. *Magn. Reson. Med.* **81**, 2614-2623 (2019).
53. Wyatt, C. R., Smith, T. B., Sammi, M. K., Rooney, W. D. & Guimaraes, A. R. Multi-parametric T2* magnetic resonance fingerprinting using variable echo times. *NMR Biomed.* **31**, e3951 (2018).
54. Krauss, W., Gunnarsson, M., Andersson, T. & Thunberg, P. Accuracy and reproducibility of a quantitative magnetic resonance imaging method for concurrent measurements of tissue relaxation times and proton density.

*Magn. Reson. Med.* **33**, 584-591 (2015).
55. Fischl, B. FreeSurfer. *Neuroimage* **62**, 774-781 (2012).
56. Desikan, R. S. *et al.* An automated labeling system for subdividing the human cerebral cortex on MRI scans into gyral based regions of interest. *NeuroImage* **31**, 968-980 (2006).
57. Cohen-Adad, J. *et al.* T2* mapping and B0 orientation-dependence at 7 T reveal cyto-and myeloarchitecture organization of the human cortex. *Neuroimage* **60**, 1006-1014 (2012).
58. Skare, S. *et al.* A 1-minute full brain MR exam using a multicontrast EPI sequence. *Magn. Reson. Med.* **79**, 3045-3054 (2018).
59. Andre, J. B. *et al.* Toward quantifying the prevalence, severity, and cost associated with patient motion during clinical MR examinations. *J. Am. Coll. Radiol.* **12**, 689-695 (2015).
60. Ing, C. *et al.* Long-term differences in language and cognitive function after childhood exposure to anesthesia. *Pediatrics* **130**, e476-e485 (2012).
61. Lutti, A., Dick, F., Sereno, M. I. & Weiskopf, N. Using high-resolution quantitative mapping of R1 as an index of cortical myelination. *Neuroimage* **93**, 176-188 (2014).
62. Waehnert, M. D. *et al.* A subject-specific framework for in vivo myeloarchitectonic analysis using high resolution quantitative MRI. *NeuroImage* **125**, 94-107 (2016).
63. Warntjes, M., Engström, M., Tisell, A. & Lundberg, P. Modeling the presence of myelin and edema in the brain based on multi-parametric quantitative MRI. *Front. Neurol.* **7**, 16 (2016).
64. Haast, R. A., Ivanov, D., Formisano, E. & Uludağ, K. Reproducibility and reliability of quantitative and weighted T1 and T2∗ mapping for myelin-based cortical parcellation at 7 Tesla. *Front. Neuroanat.* **10**, 112 (2016).
65. Marques, J. P., Khabipova, D. & Gruetter, R. Studying cyto and myeloarchitecture of the human cortex at ultra-high field with quantitative imaging: R1, R2* and magnetic susceptibility. *Neuroimage* **147**, 152-163 (2017).
66. Carey, D. *et al.* Quantitative MRI provides markers of intra-, inter-regional, and age-related differences in young adult cortical microstructure. *Neuroimage* **182**, 429-440 (2018).
67. Trampel, R., Bazin, P.-L., Pine, K. & Weiskopf, N. In-vivo magnetic resonance imaging (MRI) of laminae in the human cortex. *NeuroImage* **197**, 707-715 (2019).
68. Glasser, M. F., Goyal, M. S., Preuss, T. M., Raichle, M. E. & Van Essen, D. C. Trends and properties of human cerebral cortex: correlations with cortical myelin content. *Neuroimage* **93**, 165-175 (2014).
69. Annese, J., Pitiot, A., Dinov, I. & Toga, A. A myelo-architectonic method for the structural classification of cortical areas. *NeuroImage* **21**, 15-26 (2004).
70. Wattjes, M. *et al.* Double inversion recovery brain imaging at 3T: diagnostic value in the detection of multiple sclerosis lesions. *Am. J. Neuroradiol.* **28**, 54-59 (2007).
71. Calabrese, M. *et al.* Detection of cortical inflammatory lesions by double inversion recovery magnetic resonance imaging in patients with multiple sclerosis. *Arch. Neurol.* **64**, 1416-1422 (2007).
72. Hilbert, T. *et al.* Magnetization transfer in magnetic resonance fingerprinting. *Magn. Reson. Med.* **84**, 128-141 (2020).
73. Wang, F. *et al.* Echo planar time-resolved imaging (EPTI). *Magn. Reson. Med.* **81**, 3599-3615 (2019).
74. Boyd, S., Parikh, N., Chu, E., Peleato, B. & Eckstein, J. Distributed optimization and statistical learning via the alternating direction method of multipliers. *Faund .Trends. Mach. Learn.* **3**, 1-122 (2011).
75. Uecker, M. *et al. In Proc. Intl. Soc. Mag. Reson. Med.* **26**, 2802 (2015)
76. Tamir, J. I., Ong, F., Cheng, J. Y., Uecker, M. & Lustig, M. *In ISMRM Workshop on Data Sampling & Image Reconstruction, Sedona, 2016.*
77. Jenkinson, M., Beckmann, C. F., Behrens, T. E., Woolrich, M. W. & Smith, S. M. Fsl. *NeuroImage* **62**, 782-790 (2012).
78. Jenkinson, M., Bannister, P., Brady, M. & Smith, S. Improved optimization for the robust and accurate linear registration and motion correction of brain images. *Neuroimage* **17**, 825-841 (2002).
79. Jenkinson, M. & Smith, S. A global optimisation method for robust affine registration of brain images. *Med. Image Anal.* **5**, 143-156 (2001).
80. Waehnert, M. *et al.* Anatomically motivated modeling of cortical laminae. *Neuroimage* **93**, 210-220 (2014).

# Supplementary Information

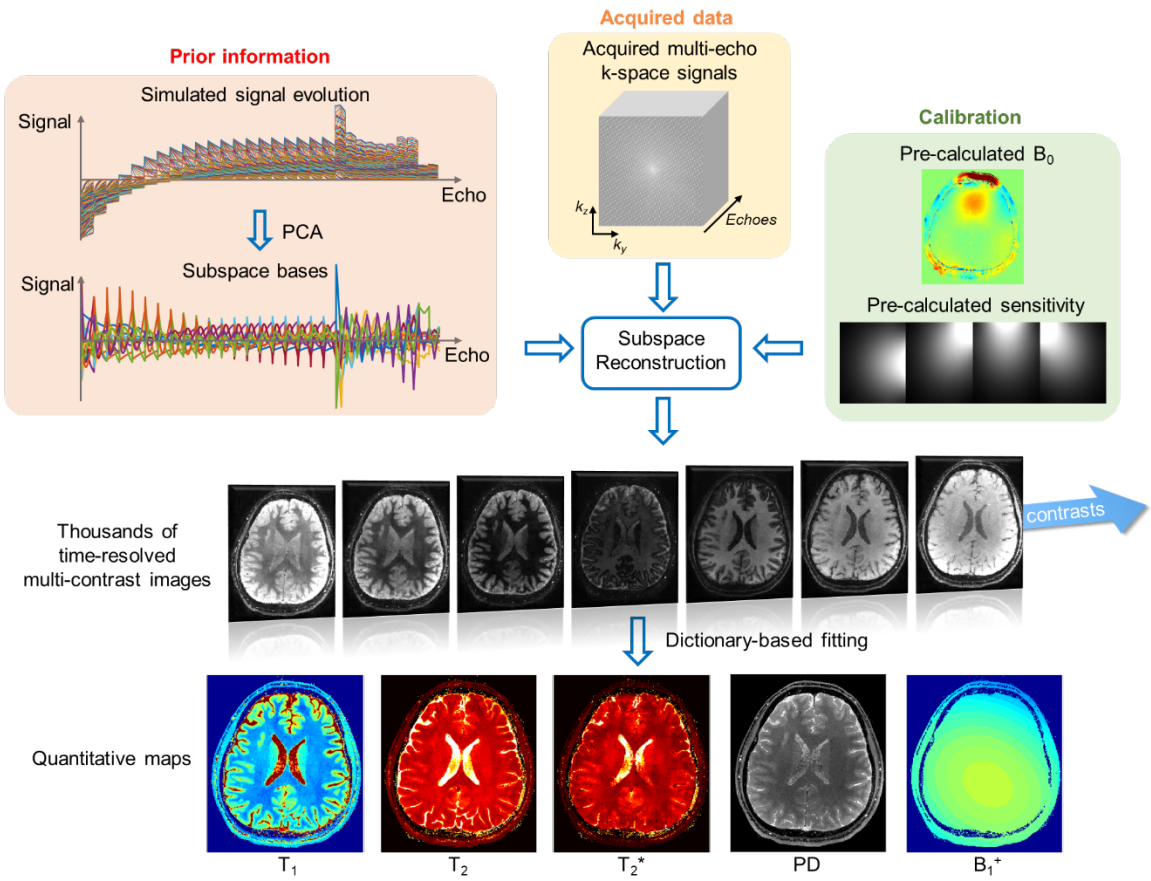


Supplementary Figure 1. Illustration of the reconstruction framework of 3D-EPTI using the low-rank subspace method. The signal evolutions can be represented by a linear combination of several subspace temporal bases instead of individual images, therefore reducing the number of unknowns. These subspace bases are extracted from the simulated signal space using principal component analysis (PCA). The subspace reconstruction is performed by integrating the information from a highly-undersampled spatiotemporal dataset, $B_0$ phase evolution and coil sensitivity maps obtained via a calibration dataset, and subspace bases. After the reconstruction, thousands of multi-contrast images are obtained without distortion and blurring, from which multiple quantitative parameters including $T_1$, $T_2$, $T_2^*$, PD, and $B_1^+$ can be estimated through dictionary matching.

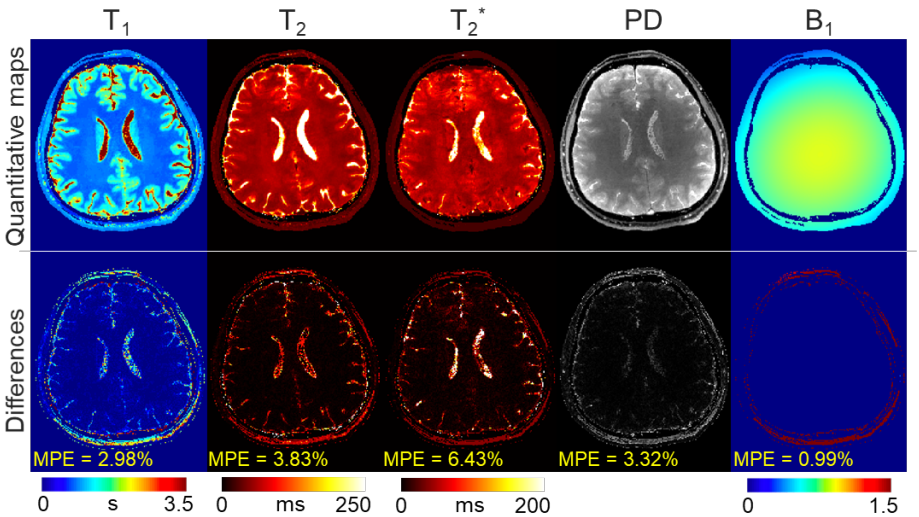


Supplementary Figure 2. Example results of the simulation experiment. The undersampled EPTI data were simulated from pre-acquired reference quantitative maps using acquisition parameters of the 1-mm 3-minute protocol. The difference maps (×2: magnified by a factor of 2) were calculated by subtracting the reference maps from the estimated quantitative maps. MPE: mean percentage error.

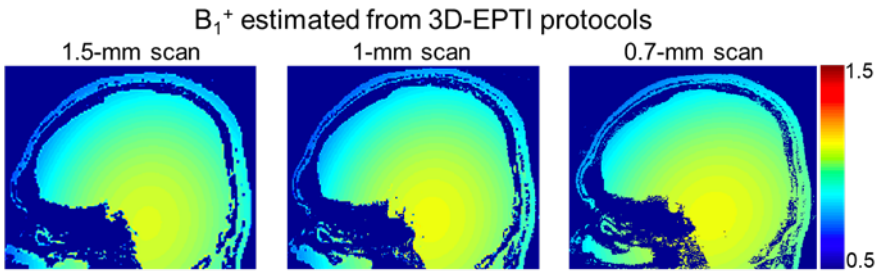


Supplementary Figure 3. The estimation of $B_1^+$ field on the same subject from three 3D-EPTI scans at different resolutions.

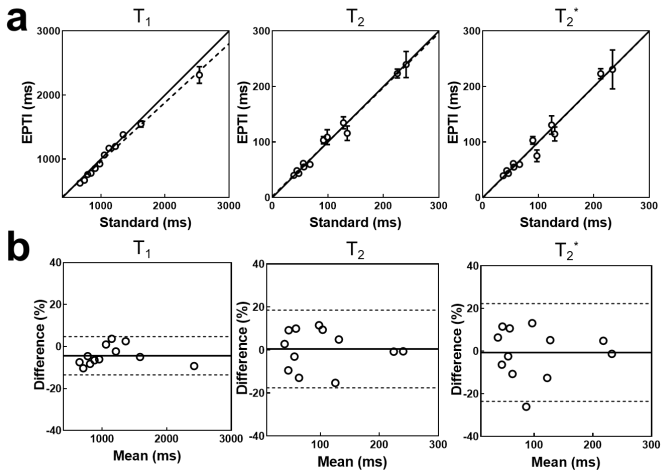


Supplementary Figure 4. Comparison of the quantitative measurements between 3D-EPTI and standard acquisitions in the phantom experiment. **a**, Scatter plots of the quantitative values in 12 selected ROIs. **b**, Bland-Alman plots of the same data.

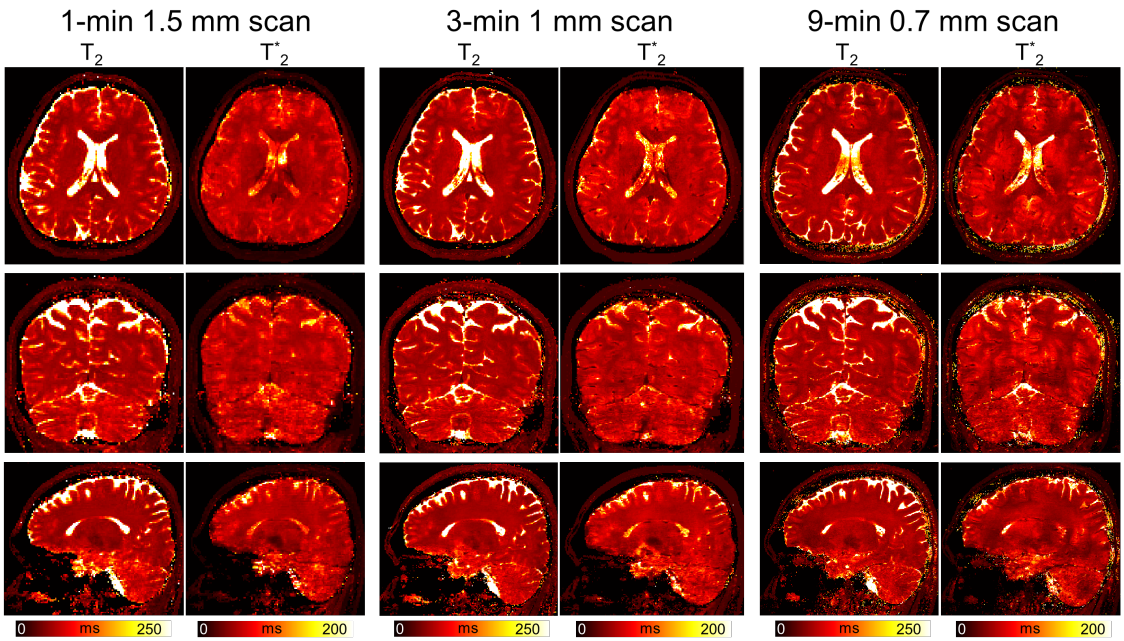


Supplementary Figure 5. The estimated $T_2$ and $T_2^*$ maps from three different protocols on the same subject. Left panel: 1-minute protocol at 1.5-mm isotropic resolution; middle panel: 3-minute protocol at 1-mm isotropic resolution; right panel: 9-minute protocol at 0.7-mm isotropic resolution.

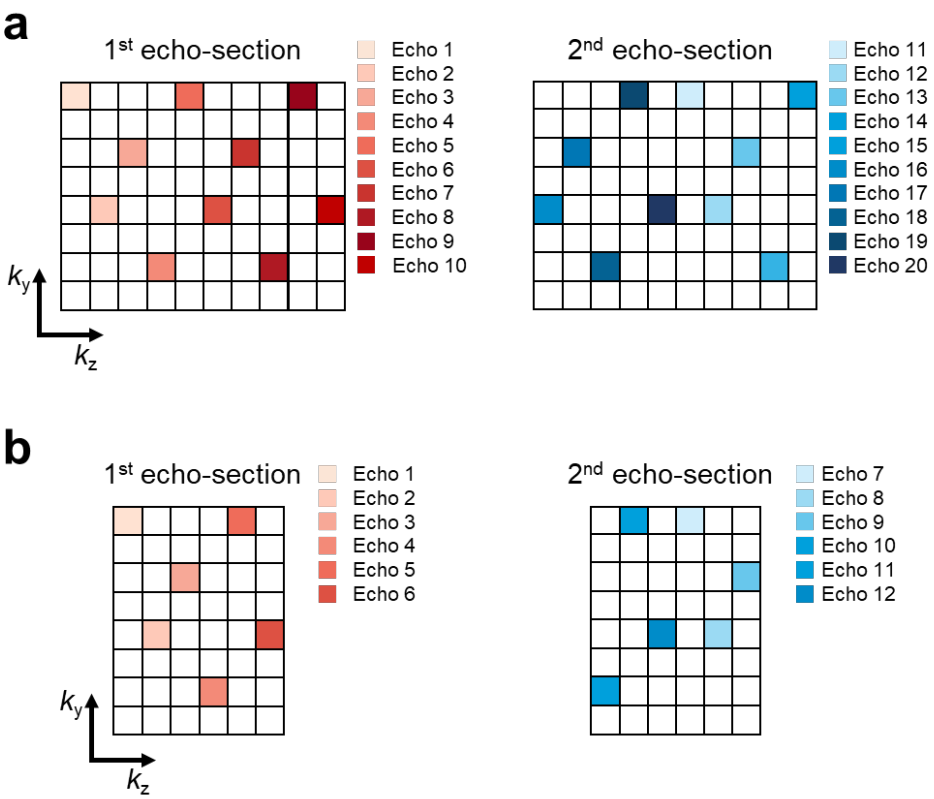


Supplementary Figure 6. The encoding patterns in $k_y$-$k_z$ space for (a) the 1.5-mm and 1-mm protocols, and (b) the 0.7 mm protocol. The different echo sections in each readout are encoded using two different patterns (red and blue) in an interleaved fashion to provide more complementary samplings (i.e., red for 1st echo section,

blue for 2nd, red for 3rd, blue for 4th, etc.).

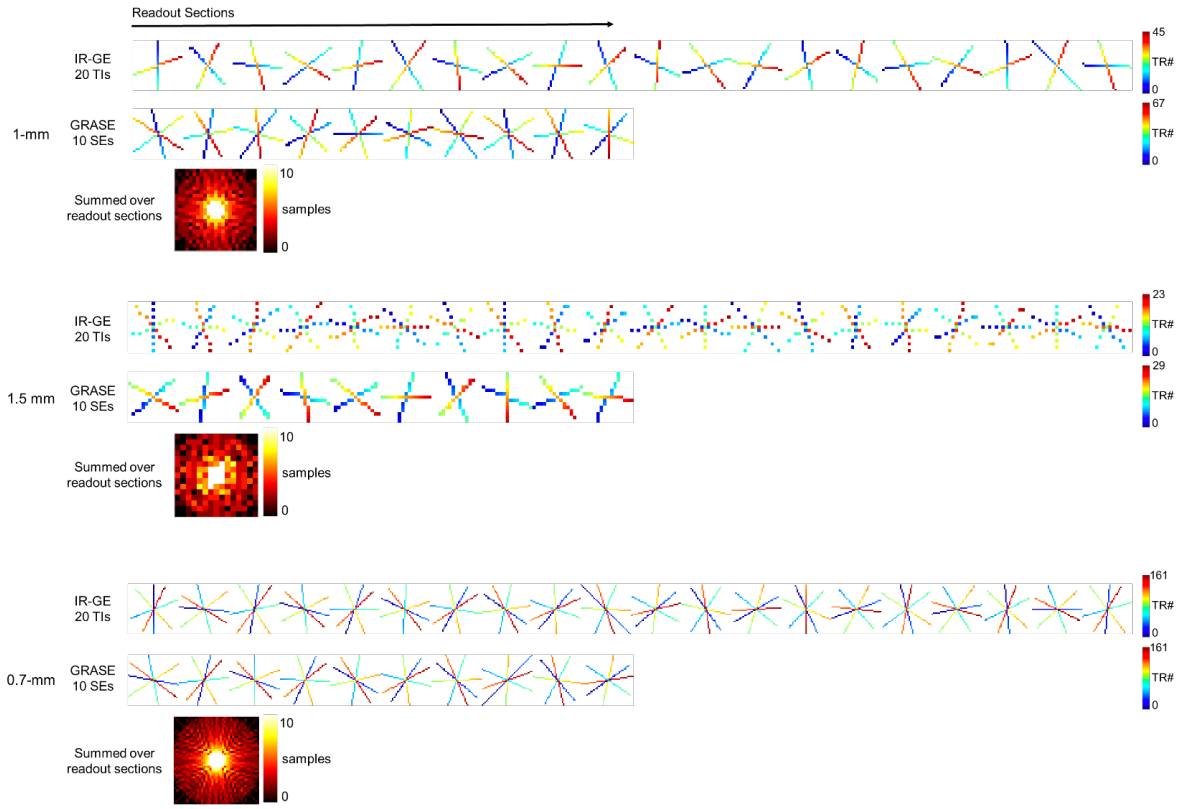


Supplementary Figure 7. The golden-angle radial-blade sampling pattern used in the designed protocols (top: 1-mm protocol, middle: 1.5-mm protocol, bottom: 0.7-mm protocol). Each color-coded point represents one sampling block acquired in a 3D-EPTI readout. After a few TRs, the sampling blocks acquired in the same readout section will form a radial-block pattern. The color coding represents the acquisition order of the blocks. For example, the index of TR (TR#) counts from 0 to the maximum, illustrated from blue to red. The combined sampling patterns across all readout sections in IR-GE and VFA-GRASE result in a variable density pattern as shown in the bottom.